Visualizing the SEI formation between lithium metal and solid-state electrolyte†

Fucheng Ren,[a] Yuqi Wu,[a] Wenhua Zuo,[b] Wengao Zhao,*[c] Siyuan Pan,[d] Hongxin Lin,[d] Haichuan Yu,[e] Jing Lin,[c] Min Lin,[d] Xiayin Yao,[e] Torsten Brezesinski,[c] Zhengliang Gong*[a] and Yong Yang*[ad]

The solid electrolyte interphase (SEI) is regarded as the most important factor affecting the durability of lithium-metal anode in all-solid-state batteries (ASSBs). Despite its significance, the nucleation and growth mechanism of SEI is not yet well understood. Here, we elucidate the thermodynamics and kinetics governing SEI formation at the Li|β-Li_3PS_4 interface at the atomic scale *via* thermodynamic phase equilibrium analysis and machine-learning-potential-assisted molecular dynamics (MD) simulations. An accurate moment tensor potential using the machine-learning method is developed for a reactive model of Li|β-Li_3PS_4. This potential enabled us to perform large-scale MD simulations with the model size expanded to the experimental dimensions (∼40 nm) while maintaining the same level of accuracy as density functional theory calculations. The results reveal a four-stage evolution process at the Li|β-Li_3PS_4 interface, namely (i) fast ion diffusion, (ii) nucleation, (iii) Li_2S growth, and (iv) stabilization. Notably, we demonstrate that the SEI can be categorized into crystalline and amorphous regions. The simulated SEI thickness, structure, and composition closely match experimental findings, validating the accuracy of the MD simulations. We further disclose the significant impact of ion diffusion kinetic limitations on the phase formation and crystallization of interfacial products. Furthermore, we shed light on the detailed potential energy (PE) distribution of lithium along the direction perpendicular to the interface. This information is crucial for better understanding interfacial ion mobility.

Broader context

All-solid-state batteries (ASSBs) with a Li-metal anode are promising next-generation energy-storage devices due to their high energy density and enhanced safety. The anode performance and durability strongly depend on the formation of the solid electrolyte interphase (SEI). Despite its significance, the fundamental understanding of SEI's chemistry, thickness, and morphology evolutions at the atomic level remains missing. Our present work visualizes and quantifies the Li|β-Li_3PS_4 interphase layer evolution process at the atomic scale for the first time by using thermodynamic phase equilibrium analysis and machine-learning-potential-assisted molecular dynamics (MD) simulations. It is worth noting that the large-scale MD simulations expand a model size close to the experimental dimensions (∼40 nm) while maintaining a comparable precision with density functional theory (DFT) calculation. Additionally, the potential energy profile of lithium throughout the SEI layer is disclosed, which is crucial to the electric double layer (EDL) and Li-ion diffusion at interface. Overall, the computational investigations offer advancements to the fundamental understanding of SEI nucleation and growth processes as well as the evolution of PE profile on the atomic scale.

Introduction

All-solid-state batteries (ASSBs) incorporating non-flammable solid-state electrolytes (SSEs) present a promising opportunity to employ lithium metal as the anode having a theoretical specific capacity of ∼3680 mA h g^{-1}.[1] This advancement has the potential to improve the energy density and safety of battery systems significantly. However, the inherent reactivity of lithium (characterized by a low reduction potential of −3.04 V *vs.* standard hydrogen electrode)[2] gives rise to interfacial reactions with the SSE, leading to the formation of a solid electrolyte

[a] *College of Energy, Xiamen University, Xiamen 361102, China. E-mail: zlgong@xmu.edu.cn*

[b] *Chemical Sciences and Engineering Division, Argonne National Laboratory, Lemont, IL, 60439, USA*

[c] *Institute of Nanotechnology, Karlsruhe Institute of Technology (KIT), 76344, Eggenstein-Leopoldshafen, Germany. E-mail: wengao.zhao@kit.edu*

[d] *State Key Laboratory for Physical Chemistry of Solid Surface, Department of Chemistry, College of Chemistry and Chemical Engineering, Xiamen University, Xiamen 361005, China. E-mail: yyang@xmu.edu.cn*

[e] *Ningbo Institute of Materials Technology and Engineering, Chinese Academy of Sciences, Ningbo 315201, P. R. China*

interphase (SEI) accompanied by an increase in cell resistance. The compatibility of the Li|SSE interface hinges on the nature of the formed phases, particularly the ionic and electronic partial conductivities. Three distinct types of interfaces between lithium and SSEs can be identified: (i) Lithium and SSE are thermodynamically stable (occurring rarely). (ii) Lithium and SSE form a mixed ionically-electronically conductive layer, which is unable to effectively passivate the interface and gradually degrades the ASSB. Examples of such SSEs include LLTO, LATP, and LGPS. (iii) Lithium and SSE form an interphase that is ionically conductive but electronically insulating, known as the Li|LiPON interface.[3] The latter type is highly desirable, as it establishes a stable interphase, thereby enabling smooth lithium transfer and ultimately enhancing cell performance. Therefore, understanding the interfacial reactions between lithium and SSEs is crucial for achieving stable and high-performance ASSBs.

The properties of the SEI, specifically its chemistry, thickness, and morphology, play important roles in determining the rate capability and durability of rechargeable batteries.[4 8] Two widely accepted models have emerged for understanding the distribution of organic and inorganic species in the SEI, namely the mosaic-type polyhetero microphase model proposed by Peled *et al.*[9] and the multilayer model proposed by Aurbach *et al.*[10] In recent years, significant efforts have been dedicated to unraveling the SEI formation mechanism using different electrolyte compositions and electrodes. These studies revealed the intricate relationship between chemistry and cell performance. Various characterization techniques, such as X-ray photoelectron spectroscopy (XPS),[11 17] nuclear magnetic resonance (NMR) spectroscopy,[18,19] time-of-flight secondary-ion mass spectrometry (ToF-SIMS),[20] Raman spectroscopy,[11,21,22] and reflection interference microscopy (RIM),[23] have been employed to thoroughly examine the physical and chemical aspects of SEI. For example, *operando* XPS studies provided insights into the uneven distribution of Li_2S and $Li_{3-x}P$ ($0 \leq x \leq 3$) in the SEI formed at the Li|Li_2S-P_2S_5 interface.[24] Pasta *et al.* discovered that the current density strongly affects the amount of reduced decomposition products (Li_3P and $Li_{3-x}P$).[25] While cryogenic electron microscopy (cryo-EM) and high-resolution transmission electron microscopy (HR-TEM) revealed the mosaic-type and multilayer structures of the SEI, crystalline $Li_{3-x}P$ ($0 \leq x \leq 3$) species have not been observed in P-containing SSE systems.[21,26 30] Despite the progress made, achieving a dynamic and comprehensive understanding of the chemistry, structure, and morphology evolution remains challenging, primarily due to the limitations of current characterization techniques. Further advancements are necessary to gain more insights into the SEI evolution, ultimately contributing to the development of more efficient and longer-lasting battery technologies.

Understanding the kinetics underlying the SEI formation is paramount. *Ab initio* molecular dynamics (AIMD) simulations have proven effective in investigating solid–solid interfacial chemistry on the atomic scale.[18,31 36] Recently, Cheng *et al.* explored the reactions at the Li|Li_6PS_5Cl interface using a model size of ~11 Å (along the *a* and *b* axes), consisting of a total of 228 atoms. They observed the decomposition of PS_4 tetrahedra near the interface, leading to the formation of Li–P and Li–S bonds.[37] Similar observations have been made for the Li|β-Li_3PS_4 interface within a simulation timeframe of 20 ps.[38] Despite these valuable insights, the limited model size and timescale of AIMD simulations remain inadequate in capturing critical variations in properties of the SEI layer observed in experimental settings. Further advancements in computational methodologies are necessary to enable more comprehensive and realistic simulations of the SEI, aligned with experimental observations.

The recently developed deep potential molecular dynamics (DeePMD) simulation scheme presents a computationally efficient and accurate solution that has gained widespread adoption in the computational chemistry.[39 41] DeePMD has demonstrated its ability to substantially increase the scale of model size and simulation time while maintaining a similar level of accuracy to density functional theory (DFT) calculations. This has opened up new possibilities for addressing the critical issues in battery research. Through its application, researchers have successfully tackled various challenges in the field of battery technology. For instance, DeePMD has shed light on the switching of the redox level of H_2O in highly concentrated electrolytes,[42] the self-healing characteristics of Li-metal systems,[43] and the lithium diffusion mechanism in both amorphous LiF and Li_2CO_3.[44] By leveraging the computational efficiency and accuracy of DeePMD, it is capable of tackling the remaining challenges in the battery field with a larger scope and longer simulation times, thus improving understanding of battery phenomena and guiding the development of advanced energy-storage technologies.

In this work, we disclose the complex mechanisms governing the formation and evolution of the SEI between lithium metal and β-Li_3PS_4, encompassing both thermodynamic and kinetic aspects. To achieve this, we exploit DeePMD simulations, allowing to significantly expand the model size from the limited scale of hundreds of atoms used in DFT to a more realistic scale (>12 000 atoms), corresponding to ~40 nm. This major increase in model size provides a sufficient thickness for the simulated SEI, ensuring its representation on an experimental scale. Through direct monitoring of SEI formation and growth, our findings demonstrate a ~12.4 nm layer between Li and β-Li_3PS_4, characterized by two distinct regions, namely a crystalline (Li_2S of thickness ~5.0 nm adjacent to Li) and an amorphous one (near the β-Li_3PS_4). Moreover, the formation of $Li_{3-x}P$ ($0 \leq x \leq 3$) phases has been identified as being thermodynamically favorable; their crystallization is hindered by steric effects (diffusion limitations). In addition, we reveal the potential energy (PE) distribution of lithium, unveiling two distinct drops at the Li|SEI interface (0.63 eV) and SEI|β-Li_3PS_4 interface (0.67 eV) within the respective thicknesses of 1.8 and 2.4 nm.

Results and discussion

Training a deep potential model and accuracy test

A high-quality deep potential (DP) model is proposed for a reactive solid–solid interface, encompassing descriptors for the bulk materials and the interphases formed by side reactions. The workflow for generating the reactive interface model of Li|β-Li_3PS_4 is illustrated in Fig. 1a. The DP generation process involves two key steps: bulk training for obtaining the descriptors for lithium metal and β-Li_3PS_4 by employing a 15 ps AIMD simulation as initialization (step 1). Reactive interface model training acquires the descriptors for the interphases formed due to the side reactions between Li and β-Li_3PS_4 (step 2). The initial structures for Li|β-Li_3PS_4 are depicted in Fig. S1 (ESI†), comprising various surface combinations: Li(001)|β-Li_3PS_4(100/010/001). Importantly, the datasets obtained from step 1 are integrated and added to the step 2 training, thereby enhancing the bulk description of Li and β-Li_3PS_4 in the final model of the reactive interface. The computational details can be found in the ESI.†

The performance of the obtained DP model was tested by comparing the energies and forces of structures predicted by DFT and DP, as shown in Fig. 1b and Fig. S2 (ESI†). It is worth noting that the DP model generated in the final training of the reactive interface model (step 2) was used to calculate the energy and force of the structures for Li and β-Li_3PS_4. The energies and forces predicted by DP model agree well with the DFT results; the root mean square errors (RMSEs) of energy for Li, β-Li_3PS_4, and Li|β-Li_3PS_4 are 2.14, 0.542, and 2.14 meV per atom and the RMSEs of force are 0.042, 0.029, and 0.101 eV Å^{-1}, respectively. The good match between the radial distribution function (RDF) curves for lithium metal and β-Li_3PS_4 obtained from DeePMD and AIMD simulations (see Fig. S3, ESI†) further underscores the accuracy and robustness of the established DP model.

Thermodynamic prediction of interphases formed through side reactions

As shown in Fig. 2, the P^{5+} ions present in the tetrahedral coordination (PS_4) undergo reduction to lower oxidation states, leading to the formation of an interphase containing LiP_7, LiP, Li_3P, and other species at voltages <1.71 V. Simultaneously, the S^{2-} ions directly produce Li_2S. The thermodynamic predictions agree well with the reported XPS results, where the P2p$_{3/2}$ signal at 125.8 eV and the broad peaks in the range of 129–131 eV correspond to Li_3P and partially reduced phosphorus compounds, respectively. Additionally, the S2p$_{3/2}$ signals at 161.5 eV suggest the formation of Li_2S at the Li|Li_3PS_4 interface.[45] The XPS characterizations of interphases formed at the Li|sulfide-based (thiophosphate) SSE interface, such as Li_6PS_5Cl,[15,25,46] Li_2S–P_2S_5,[24] $Li_{10}GeP_2S_{12}$,[17] and $Li_{10}SnP_2S_{12}$,[12] exhibit a high similarity in the P2p$_{3/2}$ and S2p$_{3/2}$ signals. Thermodynamically, P^{5+} is expected to be reduced to $Li_{3-x}P$ ($0 \le x \le 3$), which is supported by the XPS data. However, crystalline phases have not been observed by HR-TEM and/or cryo-TEM imaging.[21,26] This discrepancy may derive from the complex kinetics of interfacial reactions, which makes any kind of experimental tracking challenging.

Kinetics of Li/β-Li_3PS_4 interfacial reactions

Fig. 3a–g shows the stepwise formation of SEI forming between lithium metal and β-Li_3PS_4. The initial and final interface

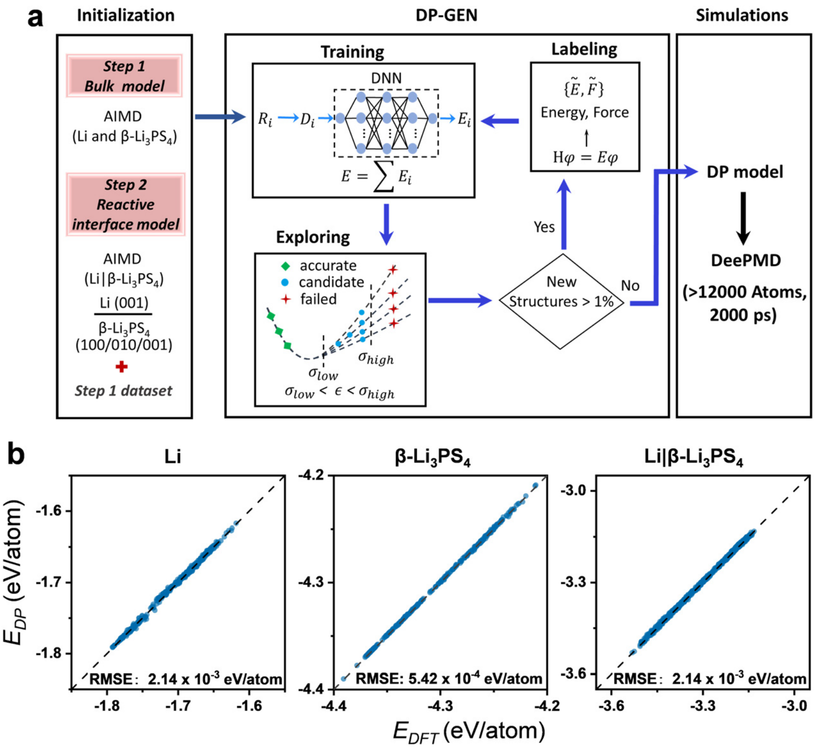

Fig. 1 (a) Workflow for the generation of DP model for lithium metal, β-Li_3PS_4 and reactive interface of Li|β-Li_3PS_4. (b) Comparison of energies of structures predicted by DP and DFT for Li, β-Li_3PS_4, and Li|β-Li_3PS_4.

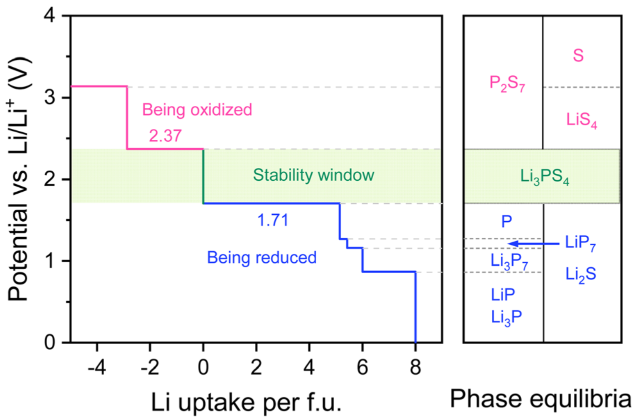

Fig. 2 Calculated thermodynamic equilibrium voltage profile and phase equilibria of β-Li_3PS_4.

structures of Li(001)|β-Li_3PS_4(010) are shown in Fig. 3a and g, respectively, with a simulation time up to 2000 ps. The formation process can be divided into four distinct stages. During the first stage, sulfur and phosphorus ions near the interface diffuse into the bulk of Li, while the lithium ions diffuse in the opposite direction, as depicted in Fig. 3b and Fig. S4 (ESI†). This mutual diffusion extends up to a depth of 4.1 nm. In the second stage, nucleation occurs at t = 306 ps, with a crystalline structure of size 1 nm emerging at the interface. Subsequently, (within 115 ps) the crystalline layer covers the Li-metal surface, reaching a thickness of 1.8 nm. The overall thickness of the crystalline region increases at a relatively slower rate, as can be seen from Fig. 3c and d. The third stage comprises the crystal growth. The lattice structure rapidly expands toward the SSE side, while the expansion toward the Li side is minimal (a visual representation is given in Movie S1, ESI†). Ultimately, the crystalline region stabilizes at a thickness of ∼5.0 nm (within 347 ps, see Fig. 3e). The fourth and final stage marks the stabilization. The symmetry of the crystalline structure increases significantly, as shown in Fig. 3f. This is in contrast to the earlier stages, where the SEI layer exhibits numerous point defects (vacancies *etc.*).

The trained reactive interface model successfully captures the description of the β-Li_3PS_4 (left), the SEI (middle), and the lithium metal (right), demonstrating the precision and robustness of the DP model (see Fig. 3g). The SEI is characterized by two distinct regions, a crystalline and an amorphous one with respective thicknesses of ∼5.0 nm and ∼7.4 nm. Notably, the crystalline region is close to the Li. The thickness and distribution of the simulated SEI are in good agreement with reported experimental findings in High-resolution TEM (∼12 nm),[20,21] providing new insight into the atomic-scale formation process in ASSBs. Moreover, the lithium atoms adjacent to the SEI become highly disordered, forming an amorphous region of thickness ∼1 nm. This disordered region arises from the lattice mismatch between the Li metal and the (crystalline) SEI. A detailed analysis reveals a highly symmetric distribution of sulfur and lithium sites in the lattice region, as shown in Fig. 3h. The site distribution is consistent with the surface structures of Li_2S ($Fm\bar{3}m$ space group, mp-1153) along 101/110/011 and 100/010/001. The formed interphases and their distribution were further probed by ToF-SIMS depth profiling (see Fig. S6, ESI†), with the results suggesting that the Li_2S is distributed close to the Li-metal side. This observation corroborates the accuracy of DeePMD simulations in capturing the structural characteristics of the SEI. In contrast, the nucleation of $Li_{3-x}P$ ($0 \leq x \leq 3$) phases was not observed in the simulations. This aspect will be discussed later.

The reactivity of different surface structures [Li(001)|β-Li_3PS_4(100/010/001)] was also investigated, as shown in Fig. S7 (ESI†). The thickness of the SEI layer is found not to vary much, ranging from ∼12.4 nm to ∼13.6 nm. Moreover, the sizes of the crystalline and amorphous regions in the SEI remain close. Similar reaction features are observed along different surfaces, as illustrated in Fig. 4. The interfacial reaction between Li(001) and β-Li_3PS_4(100/001) also undergoes four stages. The formation of Li_2S follows a two-step process, as mentioned above. Firstly, the crystalline phase rapidly extends parallel to and covers the Li-metal surface with a slight increase in thickness. Subsequently, it expands toward the SSE side (see Fig. 4a and Movie S1, ESI†). The SEI on the different surfaces of β-Li_3PS_4 exhibits a similar structure, comprising again an amorphous and a crystalline region. The lithium atoms near the Li|SEI interface become highly disordered due to lattice mismatch (see Fig. 4b and Fig. S7, ESI†). The thickness of the disordered region at the Li|Li_2S interface (∼1 nm) is comparable to that of the Li|Li_2O interface (∼0.92 nm).[47] However, the different surfaces of β-Li_3PS_4 lead to varying propagation orientations of Li_2S into the SEI. This difference leads to the presence of numerous grain boundaries (major changes in the Li_2S appearance in HR-TEM images).[21]

Temperature and pressure are two critical factors that have a profound effect on the performance of batteries, and extensive investigations have been undertaken in this regard.[4,48 52] Notably, the SEI increases in thickness with increasing temperature. For instance, the thickness of the crystalline (Li_2S) and amorphous regions increases from ∼5 nm to ∼8.7 nm and from ∼7.4 nm to ∼11.9 nm, respectively, as the temperature rises from 300 to 600 K (see Fig. S8, ESI†). This trend aligns well with cryo-TEM results reported in the literature.[21,53] An increase in SEI thickness leads to a corresponding increase in impendence,[21] which can affect the battery's overall cyclability. Regarding pressure, the investigations indicate that it exerts a minimal effect on the formation process of the SEI. Comparing the size of the crystalline and amorphous regions at 0 and 100 bar, no significant differences are observed (see Table S1, ESI†). However, it should be noted that the applied pressure improves the contact between the Li and the SSE/SEI, ensuring robust ion conduction in the interphase during cycling.

The ion diffusivity during the SEI formation

The ion diffusion at the interface plays an important role in describing the kinetics of interfacial reactions. The diffusion coefficients of lithium, phosphorus, and sulfur ions were monitored throughout the whole process (*via* the mean squared displacement [MSD]), as shown in Fig. 5a. The ion diffusion exhibits significant variations and can be divided into three

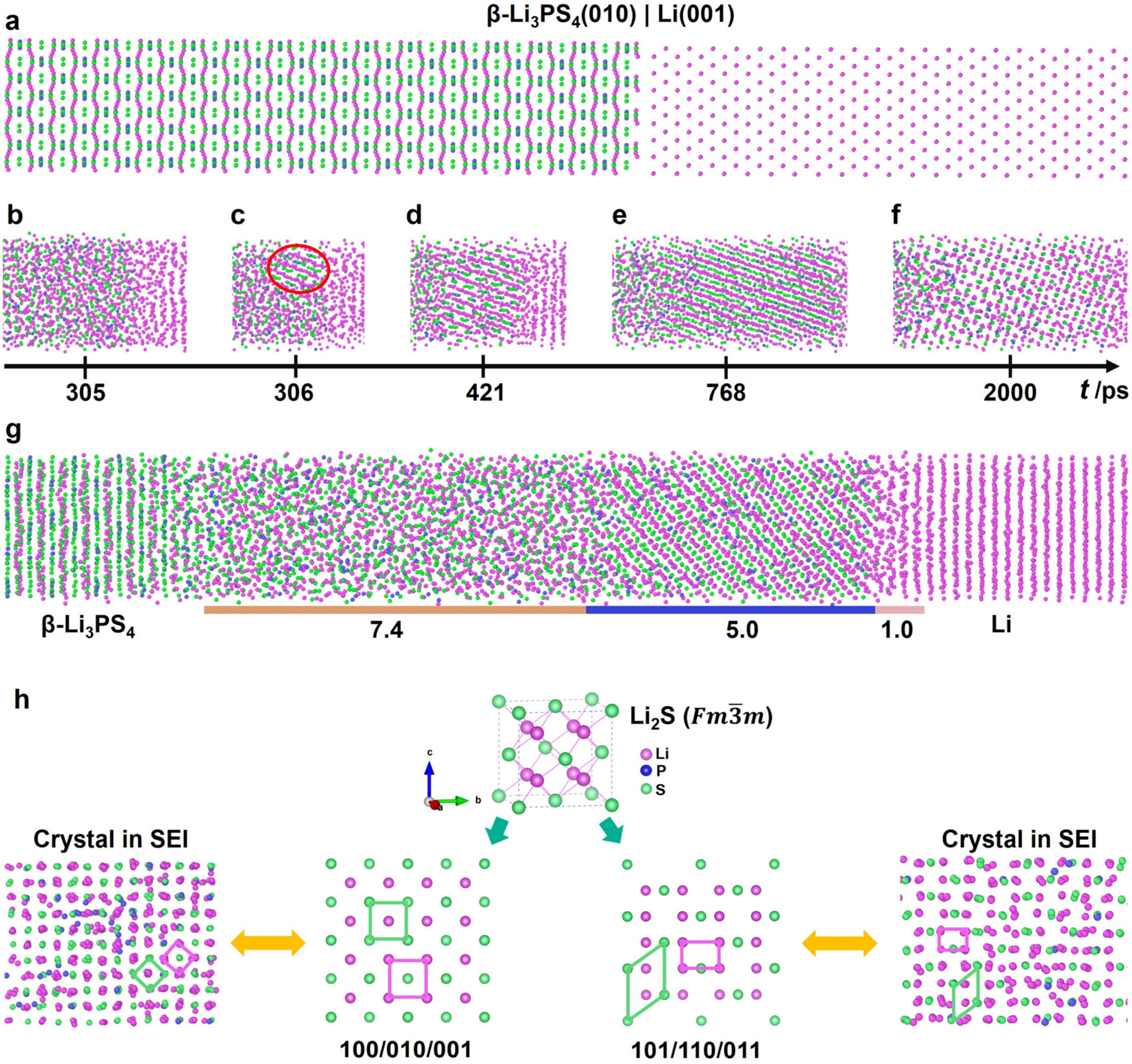

Fig. 3 SEI layer formation process between Li(001) and β-Li_3PS_4(010) at 300 K and 100 bar. (a) Initial interface model, (b) ion diffusion, (c) and (d) nucleation [the crystalline region indicated in (c) is the nucleation region], (d) and (e) crystal growth, (e) and (f) stabilization, and (g) final structure of the reactive interface model. The interface structures (b)–(f) at different simulation times are presented in Fig. S5 (ESI†). (h) Structure of the crystalline SEI region along different directions and surface structure of Li_2S with space group $Fm\bar{3}m$ along 101/110/011 and 100/010/001.

distinct regions. During the mutual ion-diffusion stage, ions close to the interface display high diffusivity, characterized by large diffusion coefficients. The phosphorus and sulfur ions rapidly diffuse into the bulk of Li with a diffusion depth of 4.1 nm. In the Li_2S formation stage, the latter ions exhibit limited diffusion, as they participate in the formation of the crystalline phase (see Fig. 5b). Throughout this stage, the lithium, phosphorus, and sulfur diffusion coefficients decrease exponentially (*e.g.*, for Li: 0.240 → 0.084 → 0.040 $Å^2\ ps^{-1}$, for P: 0.095 → 0.029 → 0.003 $Å^2\ ps^{-1}$, and for S: 0.099 → 0.029 → 0.003 $Å^2\ ps^{-1}$). After the initial three stages of the interfacial reaction, the ion diffusivity tends to become constant. Different from 3D diffusion of Li ions, the P and S ions primarily diffuse along the z-direction, as is evident from Fig. S9 (see also Fig. S4, ESI†). Furthermore, the trajectories generated over the last 500 ps (1500–2000 ps, see Fig. S10, ESI†) reveal that the phosphorus and sulfur ions in the crystalline region become localized in (specific) small spaces, forming the lattice sites (note that the phosphorus ions are randomly distributed). In contrast, ions in the amorphous region exhibit some level of flowability, yet they remain localized in relatively larger spaces.

Evolution of ion local coordination environment

The analysis of the interfacial reactions above does not reveal the nucleation of $Li_{3-x}P$ ($0 \leq x \leq 3$) phases. However, signatures of these species are detected by XPS[12,15,17,24,25,45,46,54,55] and NMR spectroscopy,[11,18] indicating their presence and suggesting a correlation with the local coordination environments. To further examine this, the coordination environments of sulfur and phosphorus were systematically analyzed during

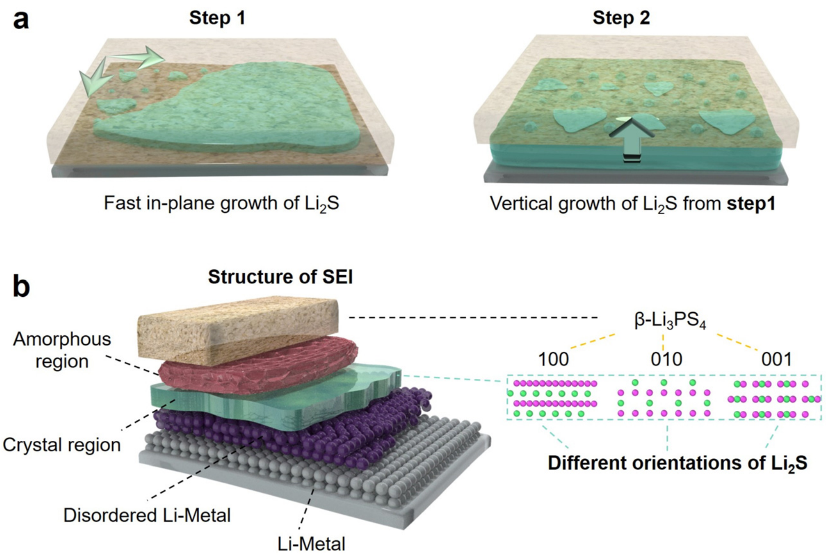

Fig. 4 (a) Illustration of the two-step growth of Li_2S at the interface. (b) Schematic diagram of the structure of the SEI formed between Li(001) and β-Li_3PS_4(100/010/001).

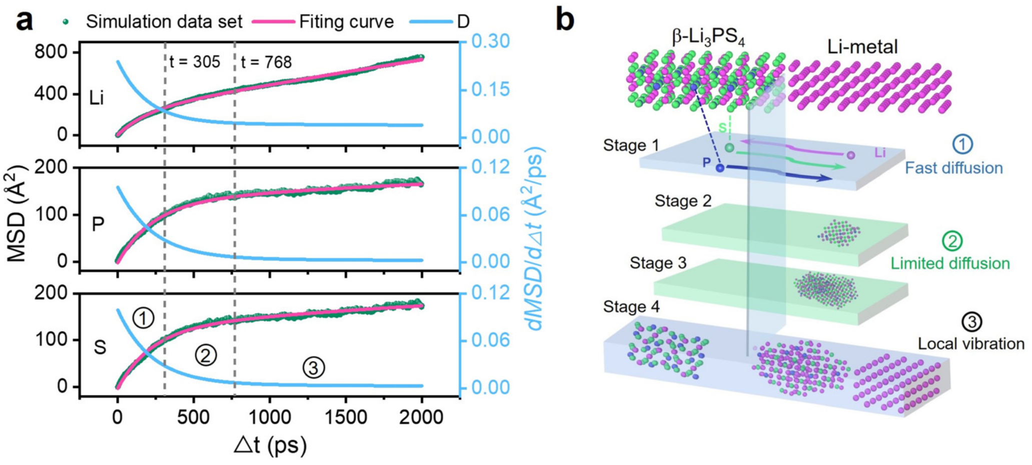

Fig. 5 (a) MSD and dMSD/$d\Delta t$ of lithium (upper), phosphorus (middle), and sulfur (bottom) ions as a function of Δt in the interface model of Li(001)|β-Li_3PS_4(010) over 2000 ps at 300 K and 100 bar. (b) Schematic of ion diffusion behavior during the SEI formation process. The dMSD/$d\Delta t$ profile in (a) can be divided into three regions (labeled in bottom) corresponding to three different diffusion behaviors in (b).

the progression of the reaction. The red lines in Fig. 6a and d depict their regular distribution along the z-direction in the bulk of β-Li_3PS_4 (along 010, see also Fig. 3a). It is evident that both sulfur and phosphorus no longer diffuse into the lithium metal once the crystalline structure is formed at t = 306 ps. The PS_4 units of β-Li_3PS_4 near the SEI|β-Li_3PS_4 interface are well preserved, with phosphorus being coordinated by four sulfur anions and only one phosphorus atom existing around each sulfur, satisfying the local environment of PS_4 (see Fig. 6g). However, when the ion diffusion occurs at the Li|β-Li_3PS_4 interface, the coordination numbers of sulfur with phosphorus and phosphorus with sulfur become zero, indicating that there is no phosphorus in the local environment of sulfur and the PS_4 units in the SEI are completely decomposed (see Fig. 6b and Fig. S11, ESI†). This structural degradation extends to the bulk of β-Li_3PS_4, accompanied by the formation of P–P bonds, with the coordination number of phosphorus with phosphorus reaching two, resulting in triangular configurations (see Fig. 6e). Some of these triangular configurations transform into tetrahedral configurations, with the coordination number increasing to three (see Fig. S12, ESI†). These configurations are the basic units that constitute the reduced side products of P^{5+}, such as LiP, LiP_3, LiP_5 *etc.* (see Fig. S12, ESI†), where the local environment of phosphorus corresponds to its coordination number with lithium and phosphorus ions. Notably, in the amorphous region close to the β-Li_3PS_4, numerous $S_3P–PS_3$ structures exist, where the coordination number of phosphorus with phosphorus and sulfur is one and three, respectively

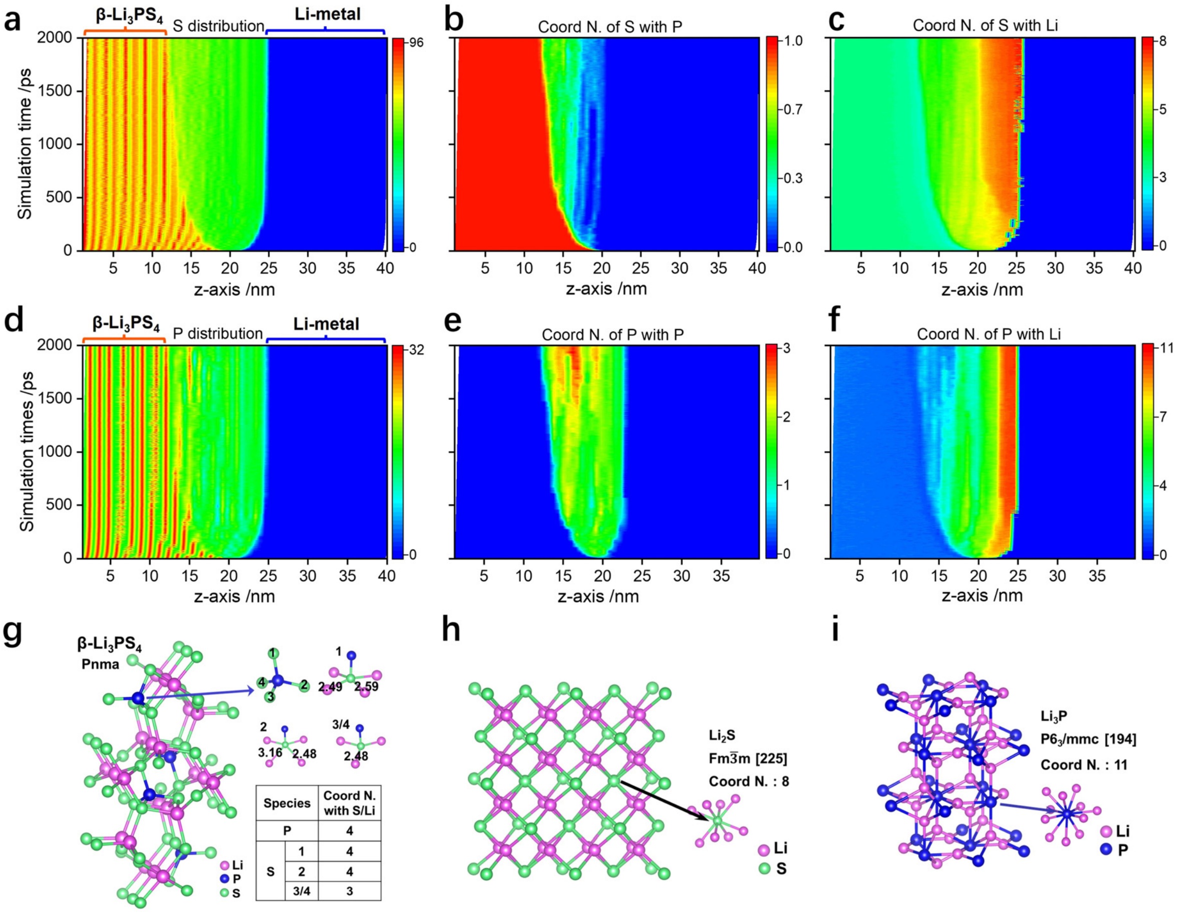

Fig. 6 (a) Sulfur and (b) phosphorus distribution along the z-direction over 2000 ps. The coordination numbers of sulfur and phosphorus with (d) and (e) phosphorus and with (c) and (f) lithium. (g)–(i) Crystal structure of β-Li_3PS_4 (g), Li_2S (h), and Li_3P (i) with the local coordination environments and numbers indicated. The partially reduced phosphorus species are presented in Fig. S11 (ESI†). The initial interface between lithium metal and β-Li_3PS_4 is located at 20.2 nm.

(see Fig. 6e and Fig. S11, ESI†). Additionally, the P-containing species in the amorphous region correspond to that detected by XPS, exhibiting $P2p_{3/2}$ signals in the binding energy range of 129–131 eV.[45]

In the crystalline region, the average coordination number of sulfur with lithium is 7.7, which is slightly lower than that expected for Li_2S (mp-1153), suggesting the presence of Li vacancies (see Fig. 6c and h). Interestingly, the size of the crystalline region remains relatively constant after the growth stage of Li_2S (see red region in Fig. 6c). As can be seen from Fig. 6f, there is also a region, where the averaged coordination number of phosphorus with lithium is 10.8, which is close to that in Li_3P ($P6_3/mmc$ space group, mp-736) (see Fig. 6i). However, they tend to remain amorphous in the SEI (instead of crystallizing with further diffusion and polymerization). This is because the triangular and tetrahedral configurations of phosphorus bonding with lithium and sulfur strongly increase the steric hindrance for diffusion.

The distribution of species in the formed interphases and their local environments were further corroborated by ToF-SIMS and solid-state NMR spectroscopy (more details in the ESI†). The results from these measurements are presented in Fig. S6 and S13 (ESI†). From ToF-SIMS depth profiling, it is evident that the LiS^- and Li^- signals show the same tendency, whereas S^{3-}, LiS_2^- and LiS_3^- reveal the opposite trend from β-Li_3PS_4 to Li, thus indicating that Li_2S distributes close to the Li-metal side. The intensity of the LiP^- signal also shows the same tendency as that for LiS^- and Li^-, while LiP_4^- and $Li_2P_2^-$ display the opposite trend, suggesting that P close to the Li metal has little coordination with itself, unlike at the β-Li_3PS_4 side, which agrees with the simulation results. Due to the complex environment of the P-containing species in the SEI layer, a broadened ^{31}P NMR peak appears at $^-330$ ppm, suggesting the local environment of P being consistent with that of amorphous Li_3P (^7Li peak at 6.5 ppm).

Additionally, the analysis of phosphorus and sulfur counting in the final structure (along the z-axis, see Fig. S14, ESI†) reveals a gradual decrease from β-Li_3PS_4 to Li. This observation is in good agreement with results from XPS depth profiling.[45] Overall, the simulation results help explain the observed discrepancy between spectroscopy and electron microscopy characterizations.[18,21,26,45]

Evolution of lithium potential energy distribution throughout the SEI layer

The electrical double layer (EDL) is an important feature of all electrochemical interfaces, controlling the kinetics and

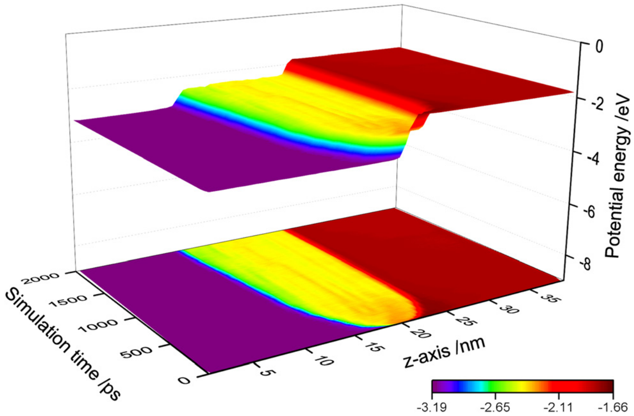

Fig. 7 The evolution of the PE profile of lithium along the *z*-direction within the simulation time scale of 2000 ps.

thermodynamics of both electron and ion transfer at the interface. It has been widely investigated by constructing and designing different models and experiments.[56–63] The potential energy (PE) distribution is crucial for the EDL and affects the Li-ion conduction. Using the reactive interface structures developed in this work allowed directly studying the PE distribution of lithium throughout the SEI and visualizing the evolution of the PE profile during the whole process. Fig. 7 shows the PE distribution along the *z*-axis of the interfacial structure and its evolution. As can be seen, the PE of lithium in the bulk of Li and β-Li_3PS_4 is constant, while there exists two large drops at the Li|SEI and SEI|β-Li_3PS_4 interfaces (note that the PE slightly decreases from the crystalline region to the amorphous one). The small fluctuations in the SEI are due to the complex structure comprising various species, such as Li_2S, $Li_{3-x}P$ ($0 \leq x \leq 3$), P_xS_y *etc.*

The PE of lithium in the initial and final interfacial structures is further elucidated (see Fig. S15, ESI†). In the initial structure, a significant PE drop occurs at the Li|β-Li_3PS_4 interface (1.42 eV, 2.4 nm), which is a great driving force for inducing side reactions. Finally, this drop translates into two smaller PE drops at the SEI|β-Li_3PS_4 and Li|SEI interfaces, with values of 0.67 and 0.63 eV and thicknesses of 2.4 and 1.8 nm, respectively.

Conclusions

In conclusion, this study provides thorough insight into the thermodynamic and kinetic evolution of the SEI formed at the Li|β-Li_3PS_4 interface in ASSBs. By utilizing thermodynamic phase equilibrium analysis and DeePMD simulations with a large supercell containing 12 160 atoms at room temperature (300 K), we have uncovered several details about the SEI layer. The results demonstrate the formation of a ∼12.4 nm interphase comprising an amorphous (∼7.4 nm) and a crystalline region (∼5.0 nm), after complete relaxation of the structure. The thickness of SEI increases with increasing temperature (to ∼20.6 nm at 600 K). The lithium atoms next to the interface at the Li side become highly disordered, due to strong interactions between the lithium and the SEI. Based on the analysis of site distribution of lithium and sulfur ions and the local coordination environment of sulfur, the crystalline phase in the SEI is identified as being Li_2S. The local coordination environment of phosphorus in the SEI is found to be similar to that of typical $Li_{3-x}P$ ($0 \leq x \leq 3$) phases. However, the latter species tend to remain amorphous due to steric hindrance for ion diffusion. Furthermore, a large PE drop of lithium is observed at the pristine Li|β-Li_3PS_4 interface (1.42 eV, 2.4 nm), which subsequently translates into two smaller drops at the Li|SEI (0.63 eV, 1.8 nm) and SEI|β-Li_3PS_4 (0.67 eV, 2.4 nm) interfaces. The dynamic evolution of the SEI layer on the atomic scale is visualized and quantified, and the chemistry, thickness, and morphology are systematically tracked too. Notably, as a computationally efficient and accurate solution, DeePMD enabled us to extend the scale of the model size and simulation time, thereby providing new insight into variations of important properties in batteries. These findings help better understand the interfacial dynamics and structure of SEI layers formed in ASSBs, shedding light on critical factors that affect the cycling performance.

Author contributions

F. R. conceived and finished the calculations and original draft, Y. Q. W. assembled the ASSBs. H. L. finished the ss-NMR test. W.G. Z., W. H. Z., S. Y. P., J. L., and M. L. attended the revision of the manuscript. W. G. Z., T. B., Z. L. G., and Y. Y. edited and finalized the manuscript. Y. Y conducted the project administration and funding acquisition. All authors discussed the results and commented on the manuscript.

Conflicts of interest

There are no conflicts to declare.

Acknowledgements

This work was supported by the National Natural Science Foundation of China (grants no. 22261160570, 21935009, 22279108 and 22021001), and National Key Research and Development Program of China (grant no. 2021YFB2401800).

Notes and references

1 H. Wu, H. Jia, C. Wang, J. G. Zhang and W. Xu, *Adv. Energy Mater.*, 2021, **11**, 2003092.
2 S. Trasatti, *Pure Appl. Chem.*, 1986, **58**, 955–966.
3 A. M. Nolan, Y. Zhu, X. He, Q. Bai and Y. Mo, *Joule*, 2018, **2**, 2016–2046.
4 O. B. Chae and B. L. Lucht, *Adv. Energy Mater.*, 2023, **13**, 2203791.
5 J. Janek and W. G. Zeier, *Nat. Energy*, 2023, **8**, 230–240.
6 K. Xu, *J. Power Sources*, 2023, **559**, 232652.
7 Y. S. Meng, V. Srinivasan and K. Xu, *Science*, 2022, **378**, eabq3750.

8 Z. Zhang, Y. Li, R. Xu, W. Zhou, Y. Li, S. T. Oyakhire, Y. Wu, J. Xu, H. Wang, Z. Yu, D. T. Boyle, W. Huang, Y. Ye, H. Chen, J. Wan, Z. Bao, W. Chiu and Y. Cui, *Science*, 2022, **357**, 66–70.

9 E. Paled, *J. Electrochem. Soc.*, 1979, **126**, 2047–2051.

10 D. Aurbach, Y. Ein-Ely and A. Zaban, *J. Electrochem. Soc.*, 1994, **141**, L1.

11 D. H. S. Tan, E. A. Wu, H. Nguyen, Z. Chen, M. A. T. Marple, J.-M. Doux, X. Wang, H. Yang, A. Banerjee and Y. S. Meng, *ACS Energy Lett.*, 2019, **4**, 2418–2427.

12 B. S. Vishnugopi, M. T. Hasan, H. Zhou and P. P. Mukherjee, *ACS Energy Lett.*, 2023, **8**, 398–407.

13 Y. Chen, W. Li, C. Sun, J. Jin, Q. Wang, X. Chen, W. Zha and Z. Wen, *Adv. Energy Mater.*, 2020, **11**, 2002545.

14 T. Swamy, X. Chen and Y.-M. Chiang, *Chem. Mater.*, 2019, **31**, 707–713.

15 S. Wenzel, S. J. Sedlmaier, C. Dietrich, W. G. Zeier and J. Janek, *Solid State Ionics*, 2018, **318**, 102–112.

16 C. Dietrich, R. Koerver, M. W. Gaultois, G. Kieslich, G. Cibin, J. Janek and W. G. Zeier, *Phys. Chem. Chem. Phys.*, 2018, **20**, 20088–20095.

17 S. Wenzel, S. Randau, T. Leichtweiß, D. A. Weber, J. Sann, W. G. Zeier and J. Janek, *Chem. Mater.*, 2016, **28**, 2400–2407.

18 L. M. Riegger, S.-K. Otto, M. Sadowski, S. Jovanovic, O. Kötz, S. Harm, L. G. Balzat, S. Merz, S. Burkhardt, F. H. Richter, J. Sann, R.-A. Eichel, B. V. Lotsch, J. Granwehr, K. Albe and J. Janek, *Chem. Mater.*, 2022, **34**, 3659–3669.

19 Q. Pang, X. Liang, A. Shyamsunder and L. F. Nazar, *Joule*, 2017, **1**, 871–886.

20 S.-K. Otto, L. M. Riegger, T. Fuchs, S. Kayser, P. Schweitzer, S. Burkhardt, A. Henss and J. Janek, *Adv. Mater. Interfaces*, 2022, **9**, 2102387.

21 S. Luo, X. Liu, X. Zhang, X. Wang, Z. Wang, Y. Zhang, H. Wang, W. Ma, L. Zhu and X. Zhang, *ACS Energy Lett.*, 2022, **7**, 3064–3071.

22 J. Nanda, G. Yang, T. Hou, D. N. Voylov, X. Li, R. E. Ruther and A. P. Sokolov, *Joule*, 2019, **3**, 2001–2019.

23 G. Feng, H. Jia, Y. Shi, X. Yang, Y. Liang, M. H. Engelhard, Y. Zhang, C. Yang, K. Xu, Y. Yao, W. Xu and X. Shan, *Nat. Nanotechnol.*, 2023, **18**, 780–789.

24 K. N. Wood, K. X. Steirer, S. E. Hafner, C. Ban, S. Santhanagopalan, S. H. Lee and G. Teeter, *Nat. Commun.*, 2018, **9**, 2490.

25 S. Narayanan, U. Ulissi, J. S. Gibson, Y. A. Chart, R. S. Weatherup and M. Pasta, *Nat. Commun.*, 2022, **13**, 7237.

26 D. Cheng, T. A. Wynn, X. Wang, S. Wang, M. Zhang, R. Shimizu, S. Bai, H. Nguyen, C. Fang, M.-C. Kim, W. Li, B. Lu, S. J. Kim and Y. S. Meng, *Joule*, 2020, **4**, 2484–2500.

27 R. Lin, Y. He, C. Wang, P. Zou, E. Hu, X. Q. Yang, K. Xu and H. L. Xin, *Nat. Nanotechnol.*, 2022, **17**, 768–776.

28 Y. Xu, H. Wu, Y. He, Q. Chen, J. G. Zhang, W. Xu and C. Wang, *Nano Lett.*, 2020, **20**, 418–425.

29 O. Sheng, J. Zheng, Z. Ju, C. Jin, Y. Wang, M. Chen, J. Nai, T. Liu, W. Zhang, Y. Liu and X. Tao, *Adv. Mater.*, 2020, **32**, 2000223.

30 Y. Li, Y. Li, A. Pei, K. Yan, Y. Sun, C.-L. Wu, L.-M. Joubert, R. Chin, A. L. Koh, Y. Yu, J. Perrino, B. Butz, S. Chu and Y. Cui, *Science*, 2017, **358**, 506–510.

31 P. Johari, Y. Qi and V. B. Shenoy, *Nano Lett.*, 2011, **11**, 5494–5500.

32 N. D. Lepley and N. A. W. Holzwarth, *Phys. Rev. B: Condens. Matter Mater. Phys.*, 2015, **92**, 214201.

33 L. E. Camacho-Forero and P. B. Balbuena, *Chem. Mater.*, 2019, **32**, 360–373.

34 H. Tian, Z. Liu, Y. Ji, L. Chen and Y. Qi, *Chem. Mater.*, 2019, **31**, 7351–7359.

35 C. Yang and Y. Qi, *Chem. Mater.*, 2021, **33**, 2814–2823.

36 H. Tian, B. Xu and Y. Qi, *J. Power Sources*, 2018, **392**, 79–86.

37 T. Cheng, B. V. Merinov, S. Morozov and W. A. Goddard, *ACS Energy Lett.*, 2017, **2**, 1454–1459.

38 L. E. Camacho-Forero and P. B. Balbuena, *J. Power Sources*, 2018, **396**, 782–790.

39 L. Zhang, J. Han, H. Wang, R. Car and W. N. E, *Phys. Rev. Lett.*, 2018, **120**, 143001.

40 H. Wang, L. Zhang, J. Han and W. N. E, *Comput. Phys. Commun.*, 2018, **228**, 178–184.

41 T. Wen, L. Zhang, H. Wang, W. N. E and D. J. Srolovitz, *Mater. Futures*, 2022, **1**, 022601.

42 F. Wang, Y. Sun and J. Cheng, *J. Am. Chem. Soc.*, 2023, **145**, 4056–4064.

43 J. Jiao, G. Lai, L. Zhao, J. Lu, Q. Li, X. Xu, Y. Jiang, Y. B. He, C. Ouyang, F. Pan, H. Li and J. Zheng, *Adv. Sci.*, 2022, **9**, 2105574.

44 T. Hu, J. Tian, F. Dai, X. Wang, R. Wen and S.-Z. Xu, *J. Am. Chem. Soc.*, 2022, **145**, 1327–1333.

45 A. Kato, H. Kowada, M. Deguchi, C. Hotehama, A. Hayashi and M. Tatsumisago, *Solid State Ionics*, 2018, **322**, 1–4.

46 T. Hakari, M. Deguchi, K. Mitsuhara, T. Ohta, K. Saito, Y. Orikasa, Y. Uchimoto, Y. Kowada, A. Hayashi and M. Tatsumisago, *Chem. Mater.*, 2017, **29**, 4768–4774.

47 M. Yang, Y. Liu and Y. Mo, *Nat. Commun.*, 2023, **14**, 2986.

48 T. Krauskopf, F. H. Richter, W. G. Zeier and J. Janek, *Chem. Rev.*, 2020, **120**, 7745–7794.

49 A. Banerjee, X. Wang, C. Fang, E. A. Wu and Y. S. Meng, *Chem. Rev.*, 2020, **120**, 6878–6933.

50 C. Lee, S. Y. Han, J. A. Lewis, P. P. Shetty, D. Yeh, Y. Liu, E. Klein, H.-W. Lee and M. T. McDowell, *ACS Energy Lett.*, 2021, **6**, 3261–3269.

51 J.-M. Doux, Y. Yang, D. H. S. Tan, H. Nguyen, E. A. Wu, X. Wang, A. Banerjee and Y. S. Meng, *J. Mater. Chem. A*, 2020, **8**, 5049–5055.

52 R. Koerver, W. Zhang, L. Biasi, S. Schweidler, A. O. Kondrakov, S. Kolling, T. Brezesinski, P. Hartmann, W. G. Zeier and J. Janek, *Energy Environ. Sci.*, 2018, **11**, 2142–2158.

53 Y. Liu, Z. Ju, B. Zhang, Y. Wang, J. Nai, T. Liu and X. Tao, *Acc. Chem. Res.*, 2021, **54**, 2088–2099.

54 S. Wenzel, T. Leichtweiss, D. A. Weber, J. Sann, W. G. Zeier and J. Janek, *ACS Appl. Mater. Interfaces*, 2016, **8**, 28216–28224.

55 S. Wenzel, D. A. Weber, T. Leichtweiss, M. R. Busche, J. Sann and J. Janek, *Solid State Ionics*, 2016, **286**, 24–33.

56 M. W. Swift, J. W. Swiftand and Y. Qi, *Nat. Comput. Sci*, 2021, **1**, 212–220.

57 L. Wang, R. Xie, B. Chen, X. Yu, J. Ma, C. Li, Z. Hu, X. Sun, C. Xu, S. Dong, T. S. Chan, J. Luo, G. Cui and L. Chen, *Nat. Commun.*, 2020, **11**, 5889.

58 Z. Cheng, M. Liu, S. Ganapathy, C. Li, Z. Li, X. Zhang, P. He, H. Zhou and M. Wagemaker, *Joule*, 2020, **4**, 1311–1323.

59 M. W. Swift and Y. Qi, *Phys. Rev. Lett.*, 2019, **122**, 167701.

60 T. Nakamura, K. Amezawa, J. Kulisch, W. G. Zeier and J. Janek, *ACS Appl. Mater. Interfaces*, 2019, **11**, 19968–19976.

61 N. J. J. de Klerk and M. Wagemaker, *ACS Appl. Energy Mater.*, 2018, **1**, 5609–5618.

62 M. Fingerle, R. Buchheit, S. Sicolo, K. Albe and R. Hausbrand, *Chem. Mater.*, 2017, **29**, 7675–7685.

63 S. Braun, C. Yada and A. Latz, *J. Phys. Chem. C*, 2015, **119**, 22281–22288.